



HAL
open science

A Novel Conductometric Micro-sensor for Methanol Detection Based on Chitosan/Zinc Sulfide-Nanoparticles Composite Obtained by Green Synthesis

Sabri Ouni, Anis Madaci, Mohamed Haouari, Naim Bel Haj Mohamed, Francois Bessueille, Abdelhamid Elaissari, Abdelhamid Errachid, Nicole Jaffrezic-Renault

► To cite this version:

Sabri Ouni, Anis Madaci, Mohamed Haouari, Naim Bel Haj Mohamed, Francois Bessueille, et al.. A Novel Conductometric Micro-sensor for Methanol Detection Based on Chitosan/Zinc Sulfide-Nanoparticles Composite Obtained by Green Synthesis. *Journal of Inorganic and Organometallic Polymers and Materials*, 2023, 33 (8), pp.2574-2585. 10.1007/s10904-023-02696-8. hal-04497317

HAL Id: hal-04497317

<https://hal.science/hal-04497317v1>

Submitted on 9 Mar 2024

HAL is a multi-disciplinary open access archive for the deposit and dissemination of scientific research documents, whether they are published or not. The documents may come from teaching and research institutions in France or abroad, or from public or private research centers.

L'archive ouverte pluridisciplinaire **HAL**, est destinée au dépôt et à la diffusion de documents scientifiques de niveau recherche, publiés ou non, émanant des établissements d'enseignement et de recherche français ou étrangers, des laboratoires publics ou privés.

A novel conductometric micro-sensor for methanol detection based on chitosan/zinc sulfide-nanoparticles composite obtained by green synthesis

Sabri Ouni ^{a,b}, Anis Madaci ^a, Mohamed Haouari ^b, Naim Bel Haj Mohamed ^c, Francois Bessueille ^a, Abdelhamid Elaissari ^a, Abdelhamid Errachid ^a and Nicole Jaffrezic-Renault ^{a*}

^a University of Lyon, Institute of Analytical Sciences, 69100 Villeurbanne, France

^b University of Monastir, Laboratory of Advanced Materials and Interfaces (LIMA), Faculty of Sciences of Monastir, Monastir-Tunisia

^c Research Unit on Hetero-Epitaxies and Applications, Faculty of Sciences of Monastir, University of Monastir, Avenue of the Environment, 5019 Monastir, Tunisia

* *Corresponding authors E-mail: nicole.jaffrezic@univ-lyon1.fr*

Abstract

Methanol (MeOH) is largely used in industry but it is poisonous when ingested. A new microconductometric transducer is proposed for the detection of methanol vapor. The sensitive part of this methanol microsensor is prepared by the encapsulation of zinc sulfide (ZnS) nanoparticles (NPs) in chitosan. ZnS NPs were prepared through an aqueous colloidal route, *Artemisia Herba Alba* (AHA) plant extract being used as a capping agent. ZnS AHA NPs presents an average nanocrystal size of 3.93 nm with a cubic zinc blende structure. The ZnS AHA NPs were well dispersed in an electrodeposited chitosan film on interdigitated electrodes, for conductometric measurements. The ethanol, methanol and acetone gas-sensing responses of the films were measured at room temperature. The sensors' response time (t_{Rec}) for methanol is from 11 to 25 s from lower to higher concentrations. The limit of detection for methanol is 1400 ppm in the gas phase. The methanol sensor presents 3.8 times lower sensitivity for ethanol and 30 times lower sensitivity for acetone. The shelf life of the methanol sensor is one month.

Keywords: Chitosan film; ZnS nanoparticles; *Artemisia Herba Alba* extract; conductivity; methanol; gas sensor.

1. Introduction

Methanol, the simplest alcohol, is harmless on its own, but its metabolites formic acid and formate are very hazardous after ingestion [1,2]. It is well known that consuming MeOH may harm the neurological and circulatory systems permanently, leading to blindness, organ failure, or even death. It can be found in alcoholic drinks made by distillation or spontaneous fermentation. Blindness cases have been documented following the ingestion of as little as 4 mL of MeOH. It is often stated that 100 mL of consumed MeOH is the least deadly dosage [1]. MeOH is often employed as a cleaning agent and

solvent in industry, and it is an alternate energy carrier to hydrogen [3]. For repeated exposure during the working day without experiencing serious health consequences. It is thus necessary to create assays and sensors that are sensitive, reasonably priced, and easy to use for industrial laboratories, suppliers, and end users. MeOH has been identified using a variety of methods, such as gas chromatography [4], Fourier transform infrared spectrometry [5], Raman spectroscopy [6], and surface plasmon resonance [7]. These methods are not suited for routine usage because of their limitations, which include high costs and the requirement for skilled personnel. To address the issue, a gas sensor approach has been used to detect MeOH or other volatile organic chemicals (VOCs).

Numerous sensors are based on semiconducting metal oxides such as SnO₂ [8,9], ZnO [10,11], WO₃ [12]. The main drawbacks of these nanomaterials are their high working temperature and their rather poor specificity. Metal sulfides as sensing materials for gas detection have been poorly studied. By studying physical and chemical properties of nanostructured metal sulfides, it arose that such materials may be very good candidates to be further investigated in the chemoresistive gas sensing field. Indeed, by using these materials, we expect an improvement from an energy consumption point of view, both in thermal and photo-activation modes, due to their lower band-gap than for metal-oxide semiconductors [13]. The comparison between CdO and CdS, for the detection of 5 ppm ethanol, carried out at the relative best working temperature (300 °C) for both sensing materials, highlights the negligible response of CdO with respect to CdS. The response of SnS₂ sensor for 2500 ppm of methane was higher than the SnO₂ one, and the response/recovery times of SnS₂ were faster than SnO₂ [13]. The detection of methanol, ethanol and acetone was tested on different thicknesses of In₂S₃, in the range 2000 ppm to 10000 ppm (for methanol), at a working temperature of 350°C. The higher sensitivity was observed for ethanol [14]. SnS was able to detect ethanol in the range 14.86 ppm to 100 ppm at 160°C [15].

Some published gas sensors were based on ZnS nanoparticles, working as chemoresistors under thermoactivation. A study reports the ZnS quantum dots (QDs) synthesis by a hot-injection method for acetone gas sensing applications. This sensor was highly selective to acetone, at 175°C, in the range of 20 ppm to 100 ppm [16]. Novel Au nanoparticles decorated wurtzite ZnS hollow spheres (Au NPs-ZnS HSs) were successfully synthesized by simple hydrothermal and deposition-precipitation methods. The obtained chemoresistive sensor was used at 260°C for the detection of ethanol, n-propanol and n-butanol for 50 ppm concentration [17].

ZnS NPs have recently drawn special attention because of their abundance, low cost, good stability, non-toxicity, physical and chemical stability, good light UV absorption, and high catalytic efficiency [18-20]. Several chemical and physical methods are widely used to elaborate ZnS NPs like pulsed laser deposition [21], solvothermal [22], sol-gel [23] and hydrothermal [24]. Researchers have developed a new approach to synthesize functionalized ZnS NPs using capping agents. These surface capping agents bind on the surface of the nanoparticles and provide colloidal stability, passivation of surface defects, and water solubility [25]. Among the capping agents most often used, we can cite layers of organic thiol ligands such as mercaptopropionic acid [26], β -mercaptoethanol [27], thioglycerol [28], cysteine [29], glutathione [30] and thioglycolic acid [31]. However, another alternative method and technique is the biosynthesis of ZnS NPs by the green route due to its simplicity, non-toxicity, stability, and cheapness [32]. The synthesis of nanoparticles using plant extracts can potentially eliminate the problem of the organic capping agents, which are expensive and toxic, by making the nanoparticles more biocompatible. To the best of the author's knowledge, several researchers have been focused on the green synthesis of ZnS NPs by different plants like *Acalypha indica* [33], *Tridax procumbens* [33], *Abrus precatorius* [34], *Ficus Johannis* [35], *Azadirachta Indica* [36]. In this context, *Artemisia Herba-Alba* (AHA) or "desert wormwood", also known as 'Chih', is an herbaceous plant with woody, branched stems, 30–50 cm high, leafy, and a thick stump. *Artemisia Herba-Alba* is a grayish perennial dwarf shrub growing in arid climates (the Middle East and North Africa) [37]. The leaves are small, sessile, pubescent, and showy silver. The flowers are grouped in clusters and have ovoid flower heads [37]. *Artemisia* species have practical applications as food additives [38], antiviral agents [39], antimalarial agents [40], antimicrobial agents [41], anti-inflammatory agents [42], and anti-hepatotoxic agents [43]. Moreover, some *Artemisia* species have practical applications in medicine for the treatment of various diseases, such as stopping pain, invigorating blood, relieving cough, and acting as a diuretic, anthelmintic, antiallergenic, and antitoxic agent [44]. This desert wormwood has more than 160 individual components, including many essential oils, terpenoids, flavonoids, luteolin and flavones [44]. The phyto-bioactive constituents present in the aqueous extract of AHA play an important role in capping and stabilizing the biosynthesized ZnS NPs. There are several studies on green synthesis.

In this work, a rapid and new straightforward method for the green synthesis of ZnS-AHA NPs, using for the first time an extract of *Artemisia Herba Aba* is implemented, and these green nanoparticles are studied for their applications in gas sensors. ZnS-AHA NPs will be

encapsulated in a chitosan film as a conductive film deposited on an interdigitated electrode for the detection of gaseous compounds. Chitosan (CS), a natural biopolymer found in the shells of crustaceans and insects that contains functional groups such as hydroxyl (-OH) and amino (-NH₂), displays sufficient affinity to small analytes [45]. It has gained attention in recent years due to its unique properties, such as abundance, biocompatibility, biodegradability, low cost, and low toxicity [46]. Chitosan can be used as a coating material for electrodeposition due to its ability to form a film on metal surfaces. The electrodeposition of chitosan is based on its local insolubility, caused by the local increase of the pH value through the electroreduction of protons [47]. Its biocompatibility and biodegradability also make it an attractive alternative, making it applicable to electrochemical sensors [47], biosensors [48], gas sensors [49], and volatile organic compound sensors [50,51]. It presents appropriate interactions with the capped nanoparticles due to their functional groups. In this work, after morphological and spectroscopic characterizations, ZnS-AHA NPs is encapsulated in an electrodeposited chitosan film, allowing the electroaddressing of the chitosan/ZnS-NPs film on the working pair of interdigitated electrodes, the reference pair being covered with a chitosan film for differential measurements. The detection of methanol and other VOC (ethanol, acetone) were measured in the headspace of aqueous liquid mixtures, at ambient temperature.

2. Experimental

Chemicals, *Artemisia herba alba* plant extract, synthesis of AHA-capped ZnS NPs, fabrication process and packaging of micro-conductometric chips, electrodeposition of chitosan/ZnS-AHA films on the interdigitated electrodes, characterization techniques, and conductometric measurements are presented in the Supplementary Information.

3. Results and discussion

3.1. Nanoparticle characterization

3.1.1. Morphological study of ZnS-AHA NAs

FTIR spectroscopy was used to measure the vibrational frequencies of bonds in the molecules and to confirm the presence of different functional groups on the surface of ZnS nanoparticles (**Fig. 1a**). The absorption band at 540 cm⁻¹ was observed due to the Zn-S stretching vibrations [52]. The presence of Zn-S vibration clearly indicated that ZnS NPs were successfully formed. The absorption peak was observed at 3319 cm⁻¹ which is due to the alcohol/phenol group (-OH) stretching vibration [53]. The strong broad peak at 3665 cm⁻¹ at

tributed to N-H stretching mode of the secondary amides, coming particularly from the identified molecule dihydroxanthin in plant extract [54]. The peak at 2978 cm⁻¹ is probably ascribed to C-H alkene stretching, while the band at 2893 cm⁻¹ could be assigned to the C-H stretching branched alkane coming particularly from the identified molecule cis-hydroxydavanone compound of AHA extract [51]. The peak at 1575 cm⁻¹ could be due to the C=O carbonyl stretching group, and the peak at 1057 cm⁻¹ was assigned to the stretching vibrations of primary alcohol groups in the AHA extracts [55]. Hence, these two peaks confirmed the involvement of flavonoids or polyphenolic compounds in AHA-capped ZnS NPs [55]. The peaks at 1393 and 1259 cm⁻¹ corresponded to CH₃ and C-O stretching vibrations coming particularly from the identified molecule vulgarin [54]. FTIR analysis evidenced that green nanoparticles were stabilized with the major phytoconstituents of the AHA extract.

The crystal structures of the as-synthesized ZnS nanoparticles prepared using AHA as a capping agent were studied by X-ray diffraction (XRD), and the obtained XRD patterns are shown in **Fig. 1b**. The diffraction peaks are broad, confirming the nanometric size of the ZnS particles. For the phase identification, diffraction patterns of the ZnS were compared and analyzed using the diffraction standards of the wurtzite phase (JCPDS card No. 80-0020) and the zinc blende phase (JCPDS card No. 80-0007). XRD patterns can be indexed as a cubic zinc blende structure, and they appear in good agreement with JCPDS data card No. 80-0007, with prominent peaks corresponding to the reflections at the (111), (222), and (311) planes. The non-appearance of diffraction peaks related to the wurtzite phase, demonstrates that AHA capping favors the cubic structure. To better quantify the effect of the stabilizers, the nanoparticle size was estimated through the Scherrer formula [53]:

$$D = \frac{k\lambda}{\beta \cos(\theta)} \quad (1)$$

where D is the average crystallite size (Å), $k = 0.9$ is the Scherrer constant, λ is the wavelength of X-ray (1.5402 Å) Cu K α radiation, β is the full width at half maximum of the diffraction peak (in radian) and θ is the Bragg diffraction angle, respectively. The estimated average sizes of the ZnS-AHA nanocrystals were equal to 3.93 nm. The smaller size of the ZnS crystallites encapsulated by AHA extract is most likely due to strong interaction of AHA molecules with ZnS nanocrystals which makes the growth slower [56]. On the other hand, the lattice constant of cubic phase of ZnS nanocrystals can be estimated using the following expressions:

$$d_{hkl}^2 = \frac{a_c^2}{h^2+k^2+l^2} \quad (2)$$

where d_{hkl} is the inter-reticular distance for the hexagonal and cubic structure; h , k , and l are Miller indices; λ is the wavelength of the X-ray radiation; a_c is the lattice constant of cubic phase of ZnS nanocrystals. The calculated average value of the lattice parameter of AHA ZnS nanocrystals was $a = 5.4 \text{ \AA}$. Nevertheless, it should be kept in mind that the Scherrer formula considers only the size effects coming from the diffraction results, and it then offers a lower limit for the nanocrystals size and neglects the micro-strains [57,58].

Specific surface area is important characteristics of nanoparticles

The density ρ of ZnS-AHA NPs was calculated using the following expression [31]:

$$\rho = \frac{ZM}{N_A V} \quad (3)$$

Where Z is the number of atoms per unit cell, M (g mol^{-1}) is the molecular weight of the ZnS, V is the volume of the unit cell (cm^3) and N_A is the Avogadro number. The specific surface area S ($\text{cm}^2 \text{ g}^{-1}$) of ZnS nano-particles was calculated using the next equation [31]:

$$S = \frac{6}{\rho D} \quad (4)$$

Where ρ (g cm^{-3}) and D (nm) are the x-ray density of cubic or hexagonal nano-particles and the average particle size, respectively.

The specific surface area of ZnS-AHA was found to be $36.82 \text{ cm}^2 \text{ g}^{-1}$; this high specific surface area is a key factor to reaching the gas adsorption process.

Fig. 1c shows the HR-TEM images of the sample and the corresponding size distribution histogram. The aggregates could be due to high NPs concentrations (most likely during the solvent evaporation process for HR-TEM sample preparation). AHA-capped ZnS nanocrystals exhibit a spherical shape. The histogram of nanocrystals size distribution shows that the average crystal size is $4.03 \pm 0.5 \text{ nm}$. The d-spacing determined from the digital micrograph of ZnS is 0.29 nm , which is close to the spacing of (111) diffraction plane of cubic phase [59] and which shows that the growth of ZnS-AHA occurs preferentially along the direction [111], in agreement with XRD diffraction peaks (Fig. 1b), (111) peak being higher and more acute than the others. Nanocrystals elemental composition was determined by EDX; the results presented in **Fig. 1d** indicate that Zn and S are the major elemental components. The presence of C was related to the TEM grid. Other small peaks (Si and P) are also detected, probably due to residues coming from the synthesis and from the grid.

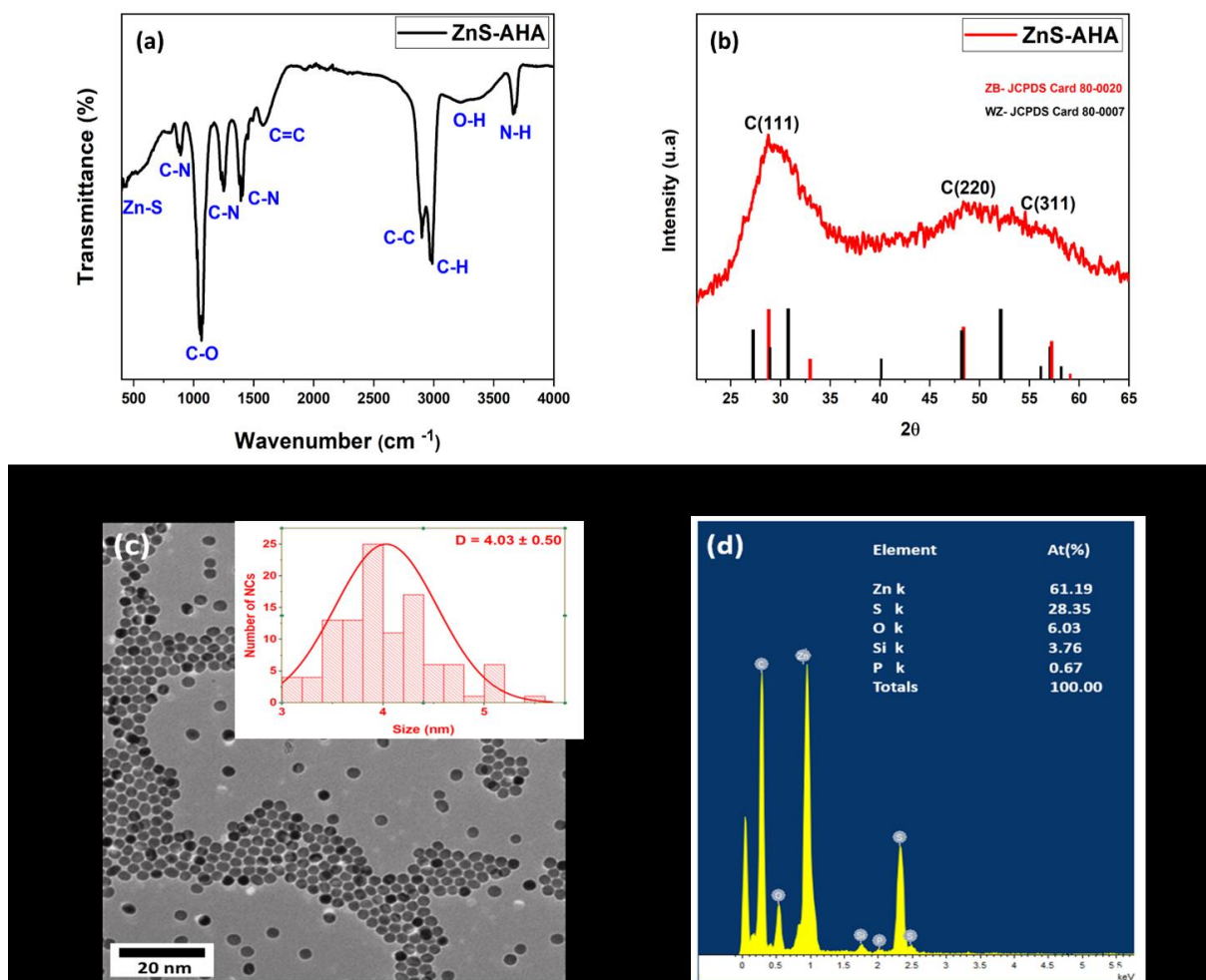


Fig. 1:(a) FTIR spectra, (b) DRX patterns, (c) HR-TEM images with inset showing the 0.29 nm lattice spacing that corresponded to the (111) plane with the size distribution of ZnS-AHA nanocrystals and (d) EDX results of ZnS-AHA NPs.

3.1.2. Optical study of ZnS-AHA NPs

In order to investigate the optical properties and the impact of the ligand on the stability and size distribution of the nanoparticles, the optical absorption spectra of the ZnS NPs dispersed in water were recorded (Fig. 2a). The UV-visible absorption spectrum of ZnS NPs suspension shows an absorption band at 325 nm related to the first electronic transition 1Se-1Sh [60]. The blue shift as compared to bulk ZnS (344 nm, $E_g = 3.6$ eV) is due to the quantum confinement

of charge carriers as a result of the small particle size. This tendency is characteristic of semiconductors II-VI, and is mainly associated with the nanocrystal size distribution and sub-band gap transitions arising from the intrinsic–extrinsic defect states. We have determined graphically the value of the optical and band-gap energy E_g using the following relation of Tauc [61]:

$$\alpha h\nu = A (h\nu - E_g)^n \quad (3)$$

Here, α is the absorption coefficient, A is a constant, h is the Planck constant, ν is the frequency of radiated photons and n is a transition-dependent factor ($n = 1/2$ for direct semiconductors). The optical gap energy of the capped ZnS NPs is obtained by extrapolating the plot of the function $(\alpha h\nu)^2$ to the value $\alpha = 0$. The intersection of the line with the horizontal axis gives the value of the band gap energy, see insert in **Fig. 2a**. The estimated band gap energy for the green ZnS is 3.70 eV. It is clear that the gap energy of these NPs shifts towards the blue compared to the bulk ZnS ($E_g = 3.6$ eV) due to the very small size of NPs, which induces a quantum confinement effect (QCE) [62].

Fig. 2b shows the emission spectra of ZnS NPs obtained with an excitation wavelength $\lambda_{exc} = 325$ nm at room temperature. An intense and wide band centered at 450 nm dominates the spectrum. The obtained emission spectra are deconvoluted using three Gaussian profiles associated with three main bands. The first band is the less intense and has a spectral width of a few nm, which is strongly correlated with the size of the nanoparticles. This band was attributed to the direct band-to-band recombination of excitons. The second emission band in the blue region (450 nm), which dominates the spectrum, was attributed to recombination between electrons and holes at the edges of the conduction and valence bands, respectively, or involved very shallow recombination centers (sulfur vacancies) [63]. Finally, the green emission band (500 nm) was attributed to the interstitial zinc atom (IZn) [22]. The FWHM of the main emission is equal to 62 nm, which is related to the size dispersion of the ZnS-AHA NPs.

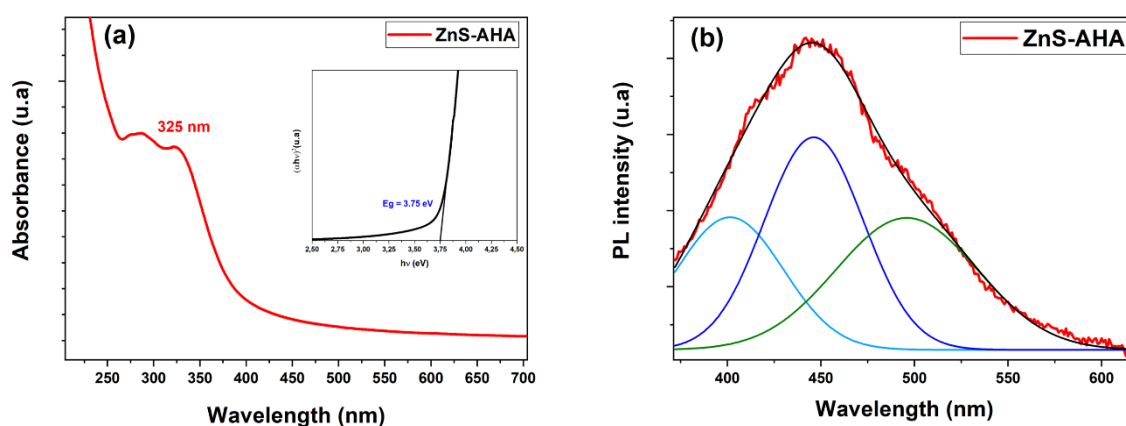


Fig. 2: (a) Absorption spectra and (b) Gaussian adjustment of PL spectra of ZnS-AHA NPs.

3.1.3. The EDS mapping of CS/ZnS

CS/ZnS is a composite consisting of a chitosan (CS) matrix combined with zinc sulfide (ZnS) nanoparticles. EDS mapping can be used to determine the spatial distribution of these elements on the micro-conductometric chips. According to **Fig. 3a**, we observe the presence of different chemical elements such as Au, Si, Ti, C, Zn, and S, which are at the origin of the deposit of CS/ZnS on the electrodes, which are already based on Au, Si, and Ti. Zn mapping (**Fig. 3b**) was obtained when focusing on the ZnKa2 Xray at 8.639 keV, which is at the foot of the AuLL Xray at 8.484 keV. A contribution of Au is then observed on the interdigitated electrodes. The dispersion of Zn is well observed between the interdigitated electrodes, in the insert of **Fig. 3b**. S mapping (**Fig. 3c**) was obtained when focusing on the Ska Xray at 2.307 keV, which is partly covered by the AuMb Xray at 2,203 keV. A contribution of Au is then observed on the interdigitated electrodes. The dispersion of S is well observed between the interdigitated electrodes, in the insert of **Fig. 3c**. EDS elemental mapping results suggest that Zn and S are homogeneously distributed on the micro-conductometric chips, showing that the AHA-ZnS NPs are well dispersed in the chitosan film.

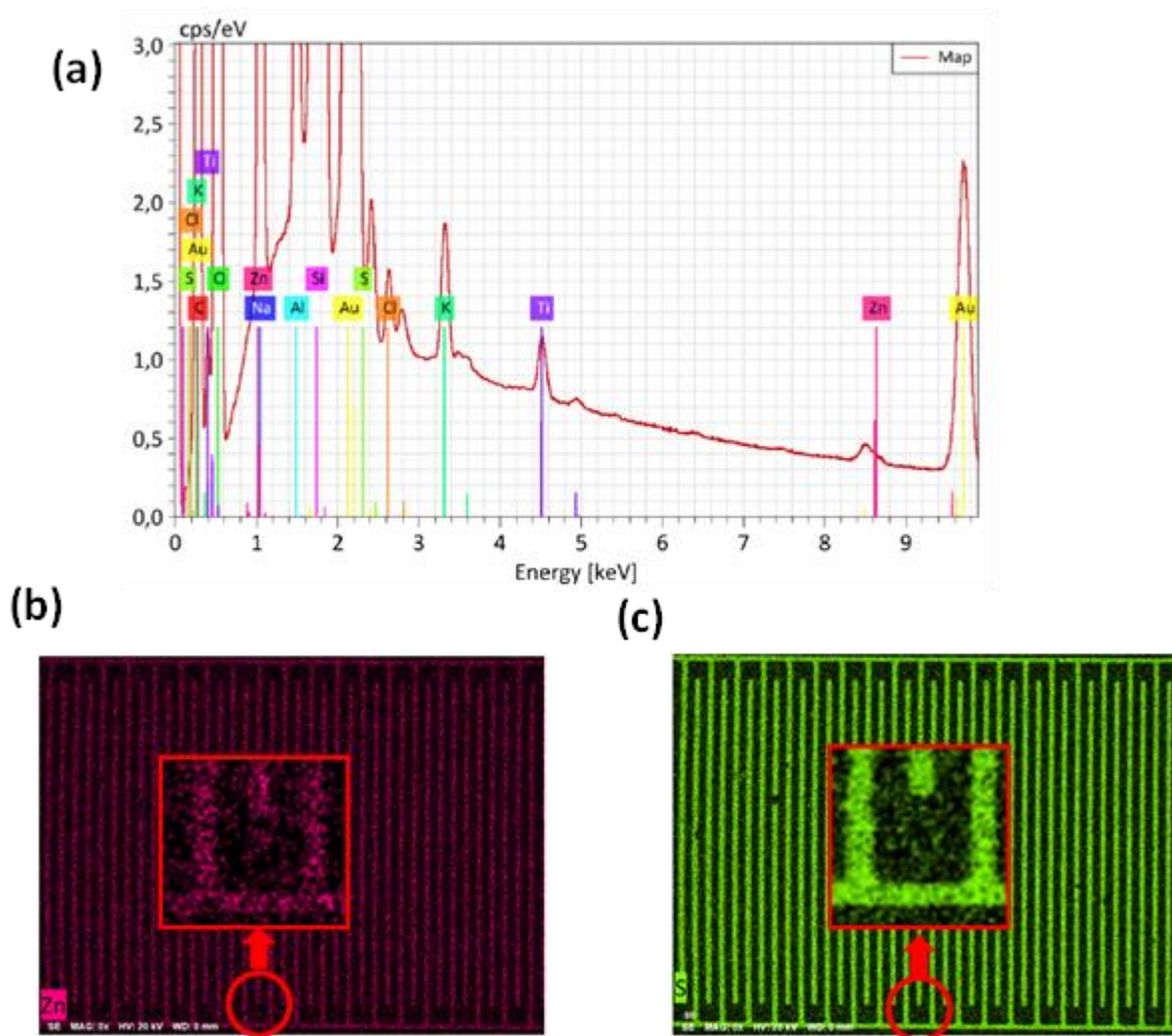


Fig.3: The EDS mapping of Chitosan/ZnS composite for atomic distribution of Zn and S. (a) EDS spectrum, (b) Zn EDS mapping, (c) S EDS mapping.

3.2. The conductometric measurements

3.2.1. Conductimetric response to vapors and proposed mechanism

The preparation of the standard solution and calculation of the gas phase content through Henry's law [64,65] are presented in **section 8** of the Supplementary Information.

To evaluate the response to target gas and to find the best gas sensing, the conductometric detection of several volatile organic compounds 'VOCs' (methanol, ethanol, acetone, chloroform and water) were performed.

The conductivity of the Chitosan-ZnS composite-based sensor, read in differential mode by the lock-in amplifier, increased dramatically when exposed to the headspace of pure solvents, as it is observed in **Fig. 4**. As clearly seen, the response of the sensor shows a higher response to methanol compared to

the other VOCs. It can be supposed that AHA-capped ZnS NPs promote surface defect formation with the creation of more active sites, which consequently enhances the gas sensing performances.

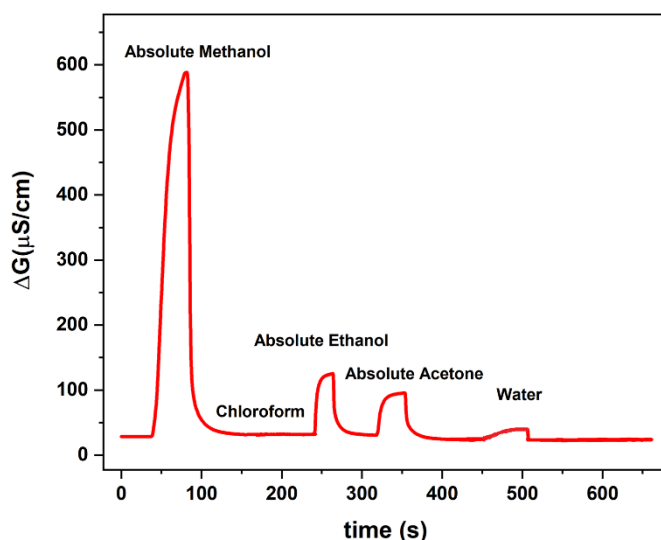
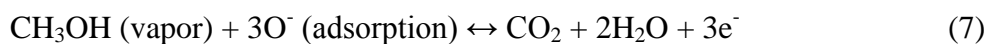


Fig. 4: Detection of gas-phase concentration for pure liquid phase of methanol, acetone, chloroform, ethanol, water

Fig. 5 describes the proposed schematic illustration of methanol gas sensing using ZnS-AHA NPs sensor. The sensing mechanism occurring during methanol detection on chitosan/ZnS-NPs sensor, can be described as follows: The first step is the oxygen adsorption on the sensor's surface, adsorbed from the outside air. The oxygen ions adsorbed on the surface of the AHA-capped ZnS NPs (Reaction (5)) and can form a depletion layer, withdrawing electrons from the bulk, which leads to an increase in the electrical resistance. O^- species are then formed (Reaction (6)). Once exposed to reducing gas (methanol, CH_3OH), O^- species will react with the gas (Reaction (7)) and enable the electrons injected back into the active material, causing an increase in electronic conductivity [66]. Recombination e^-/h^+ will then occur (Reaction (8)).



The h^+ means the holes with positive charge.

After the methanol vapor is introduced, the oxygen species containing O^- will react with gas molecules, resulting in an increase in sensor sensitivity. The high response and short response and recovery times of chitosan and ZnS-NPs are mainly based on the large surface-to-volume ratio of ZnS-AHA NPs, which is a vital factor for high sensing performance. In addition, the quantity of sulfur vacancies on ZnS-AHA NPs is also increased due to the large concentration of AHA ligand on the NPs surface. The high content of sulfide vacancies is confirmed by the photoluminescence spectra (**Fig. 2**), which are dominated by the recombination between sulfur vacancies (V_s) and the valence band. Thus, more oxygen species were adsorbed on the surface of chitosan/ZnS-NPs which yielded a greater response. The sensor response towards methanol is much higher than that towards ethanol, acetone due to the fact that the sensor works on the principle of adsorption, in which methanol has a higher polarity and less steric hindrance than ethanol or acetone. This more favorable interaction with the sensor is achieved through hydrogen bonding [67].

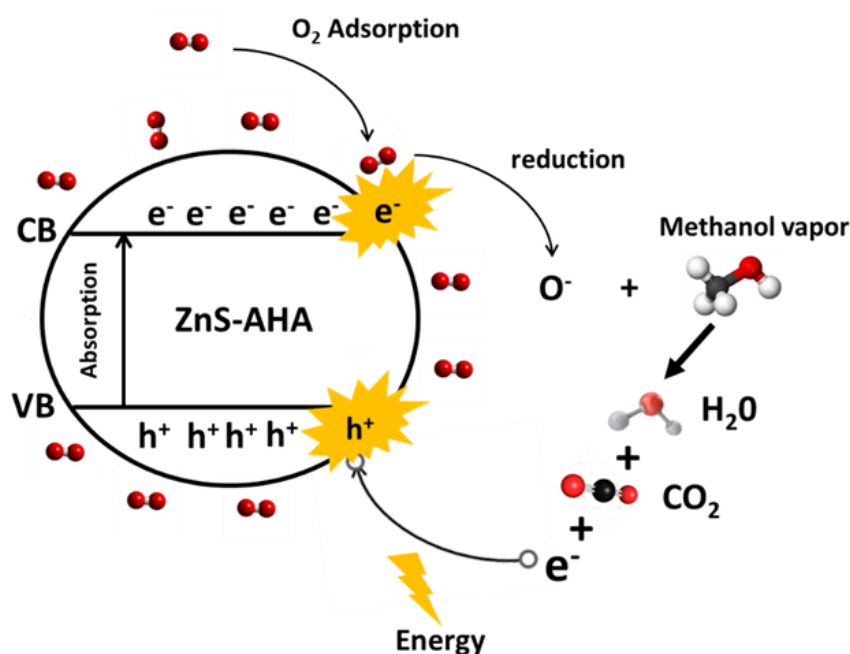


Fig. 5: Schematic illustration of methanol gas sensing using chitosan/ZnS-NPs sensor.

3.2.2. Analytical performance

Microconductometric measurements in the headspace of different methanol/water solutions are given in **Fig. 6**. It is clear that the sensor conductance increases with an increase in the concentration of methanol in the gas phase. When MeOH concentration was zero, the sensor was exposed to pure water, the recorded conductivity is 25 μS . The observed signal at 9v/v% MeOH is 450 $\mu\text{S}/\text{cm}$, the contribution of humidity would then be 5 $\mu\text{S}/\text{cm}$ (20% of water in the solution (Table S1), corresponding to 1% of the total signal, which is lower than the measured RSD. This low contribution of the water signal is due to the differential measurement system which cancel the contribution of the chitosan behaviour.

The response time (t_{Res}) of the chitosan/ZnS-NPs based conductometric sensor varies from 11 to 25 s from lower to higher concentrations (**Fig. 7**). Whereas the time to be recovered (t_{Rec}) back to the baseline, immediately after removal from the headspace, varies from 5 to 11 s. The calibration curve of the chitosan/ZnS-NPs based sensor for methanol, ethanol, and acetone are presented in **Fig. 8**. Calibration curve for methanol sensor presents the best linearity ($R^2 = 0.99988$) and the highest sensitivity S : 52.42 $\mu\text{S}\cdot\text{cm}^{-1}(\text{v}/\text{v})$, 3.8 times higher than that of ethanol (13.8 $\mu\text{S}\cdot\text{cm}^{-1}(\text{v}/\text{v})$) and 30 times higher that of acetone (1.75 $\mu\text{S}\cdot\text{cm}^{-1}(\text{v}/\text{v})$). The sensor-based on chitosan/ZnS-NPs presents a detection limit for methanol of 0.14 v/v% (1400 ppm) in the gas phase, this concentration corresponds to 0.31 M in the aqueous phase, the detection limit being calculated according to the following expression: $2\sigma/S$, σ being the noise from the blank. The relative standard deviation for the described sensor, over ten determinations, ranged from 2% for higher concentrations to around 8 % for lower concentrations. The reproducibility was studied, using 5 different methanol sensors. The obtained relative standard deviation ranges from 10 % for all concentrations.

The reusability experiment for the CS/ZnS-AHA film sensor was performed in 4 cycles with a time interval of 15 days using the absolute methanol . The main object of reusability was to investigate the results reproducibility of a methanol gas sensor. The optimum response given by CS/ZnS-AHA for methanol was 498 $\mu\text{S}\cdot\text{cm}^{-1}(\text{v}/\text{v})$ (85 %), whether the same results are reproduced by the film sensor was investigated in the experiment. With a time interval of 15 days in four turns, a slight decrease in response was observed for methanol due to visible degradation in the homogeneity of the prepared film sensor of CS/ZnS-AHA. The results obtained in the experiment are expressed in **Fig. 9**. The sensor keeps its sensitivity of detection for two months, when kept in the fridge at 4 °C between the measurements.

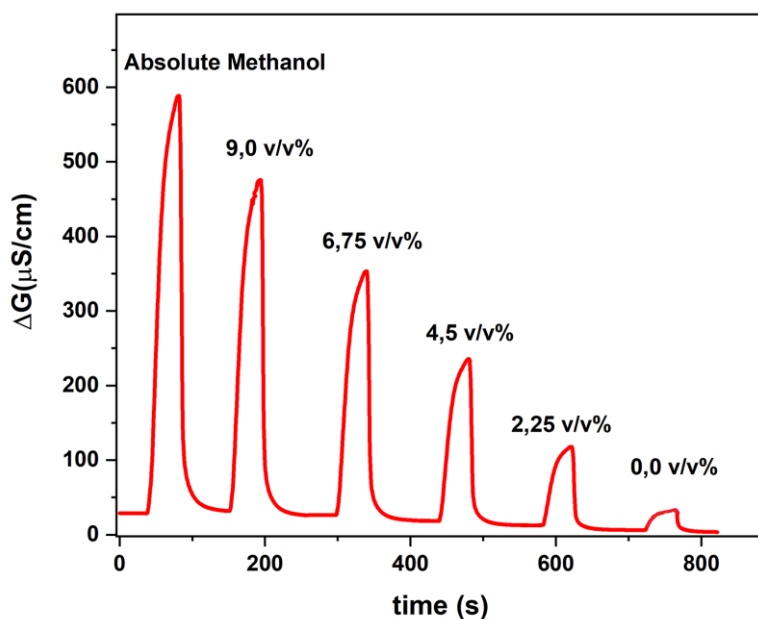


Fig. 6: Detection of gas-phase concentration for different methanol/water solutions chitosan/ZnS-NPs sensor, using a lock-in amplifier

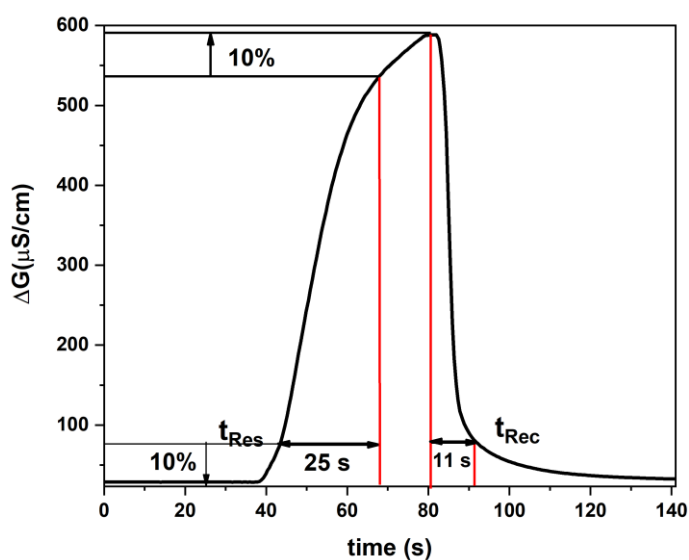


Fig. 7: Response time (t_{Res}) and recovery time (t_{Rec}) on the real-time registration of the ethanol sensor response

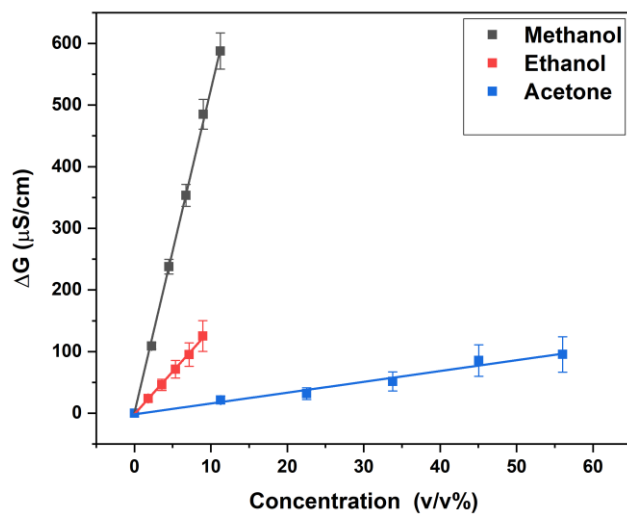


Fig. 8: Calibration curve of the gas-phase concentrations of acetone, ethanol, and methanol

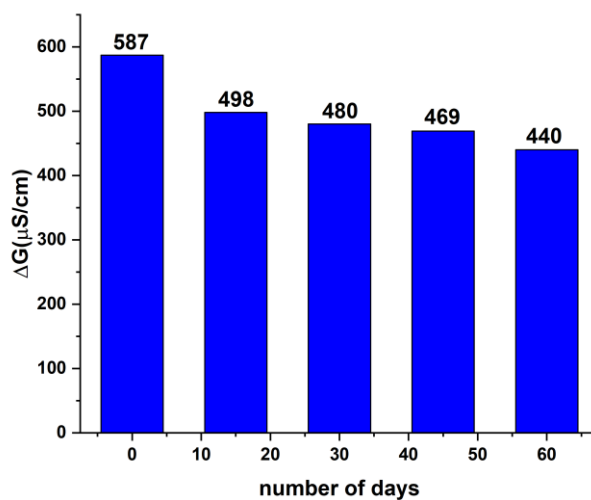


Fig.9: Reusability for Chitosan/ZnS-NPs sensor for the detection of methanol vapour in the headspace of absolute methanol

To confirm the sensor selectivity, methanol was measured in the presence of ethanol and acetone (**Fig. S5**). It is observed that the methanol signal is increased by a factor of 10% in the presence of ethanol (2%) and by a factor of 4 % in the presence of acetone (2%), which is in the range of relative standard deviation. We noticed from **Fig. 4** that the detection signal of the pure methanol gaseous phase is $587 \mu\text{S}\cdot\text{cm}^{-1}$ and that of pure water is $63 \mu\text{S}\cdot\text{cm}^{-1}$. Even

though chitosan is hygroscopic, the differential measurement decreases the signal from the water and limits its interfering effect.

A lot of methanol sensors have been fabricated (**Table 1**) but this is the first time that green synthesized ZnS-AHA is used for the conductometric detection of methanol. The obtained sensor works at ambient temperature and has a short response time. The interferences of water and of ethanol are quite limited.

Table 1: Response times and detection limits of previously published methanol sensors based on various materials.

Methanol sensors	Operating temperature (°C)	Response time (t_{Res})	Detection limit (ppm)	Refs
TiO ₂ doped CdS/amperometry	360	10 s	0.18	[68]
ADH/Amperometry	36	5 s	10	[69]
Pd doped SnO ₂ nanoparticles/ conductivity	350	25s-10s	1	[70]
graphene oxide/polyindole / conductivity	26	7	0.015	[71]
Pd–Pt–In ₂ O ₃ /SnO ₂	160	32	0.1	[72]
ZnO/MoO ₃	200	54	34	[73]
rGO–TiO ₂ nanotubes	110	41		[74]
dPIn pellet	26	26	48	[75]
PVC-NiPc nanofibers	25	13	15	[76]
Chitosan-NiPc/Conductometry	25	32s-25s	700	[77]
Chitosan-ZnS/Conductometry	25	25s-11s	1400	This work

3.2.3. Application of methanol sensor

The new standard 10% methanol ice washer is a product made from 10% methanol and used as a degreaser and windshield cleaner. After detection in the gas phase of an absolute and of a 20% methanol solution, the detection in the gas phase of the new standard 10% methanol ice washer was carried out (**Fig. S6**). The conductivity found in the ice washer gas phase was 67.1 μ S/cm. This value corresponds to 1.27 ± 0.16 v/v% in the gas phase. The determined concentration of ice washer is then 2.79 ± 0.35 M, corresponding to 11.29 ± 2.83 %, which is in good agreement with the value given by the producer, 10%.

In the same domain of gas/vapor sensors, previously published, a chemiresistor sensor based on palladium nanoparticles allows the detection of methanol in perfumes and dyes and presents a detection range of 0.31 mM–3.5 mM [78]. Our fabricated microconductometric methanol sensor is comparatively less sensitive, with a relatively large detection limit (310 mM). In order to improve the sensor's sensitivity, the gas detection could be done under UV light illumination, which may enhance the production of O⁻ species.

4. Conclusion

In summary, the present findings demonstrate the new synthesized AHA-capped ZnS NPs via a stable, simple, colloidal route at room temperature. Therefore, for the first time, an innovative green method for preparing luminescent ZnS nanoparticles was developed using *Artemisia Herba Alba*. FTIR results confirmed the functionalization of nanoparticle surfaces by AHA ligands. XRD analysis indicated the formation of nanocrystals with a cubic phase. The average size of AHA-capped ZnS nanocrystals calculated using the Debye-Scherrer formula and measured by HRTEM was around 4 nm. These new nanoparticles were used for methanol vapor detection, after their introduction in a chitosan film. The new sensor shows excellent sensitivity toward methanol—3.8 times higher than toward ethanol, 30 times higher than toward acetone. The response time (t_{90}) of the sensor varies from 11 to 25 s for lower to higher concentrations. The detection limit is 1400 ppm in the gas phase, corresponding to 0.31 M in the liquid phase. This detection limit could be improved under UV light illumination, and this sensor could then be used for the measurements of methanol in exhaled breath.

Acknowledgements

Region Auvergne Rhone-Alpes is acknowledged for the Pack Ambition International Project, EMBAI #246413. The CNRS is acknowledged for the IRP NARES. Campus France is acknowledged for the financial support through PHC Maghreb EMBISALIM. S. OUNI thanks the University of Monastir for providing the scholarship.

Conflicts of Interest: The authors declare no conflict of interest.

References

1. J.A. Kruse, Methanol poisoning, *Intensive Care Med.* **18**, 391–397 (1992). <https://doi.org/10.1007/BF01694340>
2. K.E. Hovda, O.H. Hunderi, A. Tafjord, O. Dunlop, N. Rudberg, D. Jacobsen, Methanol outbreak in Norway 2002–2004: epidemiology, clinical features and prognostic signs, *J. Intern. Med.* **258**, 181–190 (2005). <https://doi.org/10.1111/j.1365-2796.2005.01521.x>
3. F. Schorn, J.L. Breuer, R.C. Samsun, T. Schnorbus, B. Heuser, R. Peters, D. Stolten, Methanol as a renewable energy carrier: An assessment of production and transportation costs for selected global locations, *Adv. Appl. Energy.* **3**, 100050 (2021). <https://doi.org/10.1016/j.adapen.2021.100050>
4. J.A. Joseph, S. Akkermans, J.F.M. Van Impe, Processing Method for the Quantification of Methanol and Ethanol from Bioreactor Samples Using Gas Chromatography–Flame Ionization Detection, *ACS Omega.* **7**, 24121–24133 (2022). <https://doi.org/10.1021/acsomega.2c00055>

5. K. Sharma, S.P. Sharma, S. Lahiri, Novel method for identification and quantification of methanol and ethanol in alcoholic beverages by gas chromatography-fourier transform infrared spectroscopy and horizontal attenuated total reflectancefourier transform infrared spectroscopy, *J. AOAC Int.* **92**, 518–526 (2009). <https://doi.org/10.1093/jaoac/92.2.518>
6. P. Maksimov, A. Laari, V. Ruuskanen, T. Koironen, J. Ahola, Gas phase methanol synthesis with Raman spectroscopy for gas composition monitoring, *RSC Adv.* **10**, 23690–23701 (2020). <https://doi.org/10.1039/D0RA04455E>
7. S. Kumar, G. Sharma, V. Singh, Modelling of surface plasmon resonance sensor for detection of mass concentration of ethanol and methanol in a binary mixture, *Infrared Phys. Technol.* **67**, 190–196 (2014). <https://doi.org/10.1016/j.infrared.2014.07.021>
8. K.W. Khalid, A.A. Abadi, F.A. Dawood, Synthesis of SnO Nanowires on Quartz and Silicon Substrates for Gas Sensors. *J. Inorg. Organomet. Polym. Mater.* **30**, 3294–3304 (2020). <https://doi.org/10.1007/s10904-020-01617-3>
9. V. Shah, J. Bhaliya, G.M. Patel, P. Joshi, Room-Temperature Chemiresistive Gas Sensing of SnO Nanowires: A Review. *J. Inorg. Organomet. Polym. Mater.* **32**, 741–772 (2022). <https://doi.org/10.1007/s10904-021-02198-5>
10. S.T. Hezarjaribi, S. Nasirian, An Enhanced Fast EthanolSensor Based on Zinc Oxide/Nickel Oxide Nanocompositein Dynamic Situations. *J. Inorg. Organomet. Polym. Mater.* **30**, 4072–4081 (2020). <https://doi.org/10.1007/s10904-020-01556-z>
11. M. Shahabi, H. Raissi, Assessment of DFT Calculations andMolecular Dynamics Simulation on the Application of Zinc Oxide Nanotube as Hydrogen Cyanide Gas Sensor. *J. Inorg. Organomet. Polym. Mater.* **27**, 1878–1885 (2017). <https://doi.org/10.1007/s10904-017-0656-z>
12. P.S. Kolhe, P.S. Shirke, N. Maiti, *et al.* Facile Hydrothermal Synthesis of WO Nanoconifer Thin Film: Multifunctional Behavior for Gas Sensing and Field Emission Applications. *J. Inorg. Organomet. Polym. Mater.* **29**, 41–48 (2019). <https://doi.org/10.1007/s10904-018-0962-0>
13. A. Gaiardo, B. Fabbri, V. Guidi, P. Bellutti, A. Giberti, S. Gherardi, L. Vanzetti, C. Malagù, G. Zonta, Metal Sulfides as Sensing Materials for Chemoresistive Gas Sensors, *Sensors* **16**, 296 (2016) <https://doi.org/10.3390/s16030296>
14. R. Souissi, N. Bouguila, B. Bouricha, C. Vazquez-Vazquez, M. Bendahan, A. Labidi, Thickness effect on VOC sensing properties of sprayed In₂S₃ films, *RSC Adv.*, **10**, 18841 (2020). <https://doi.org/10.1039/d0ra01573c>
15. W. Shan, Z. Fu, M. Ma, Zhifu Liu, Z. Xue, J. Xu, F. Zhang and Y. Li, Facile Chemical Bath Synthesis of SnS Nanosheets and Their Ethanol Sensing Properties, *Sensors* **19**, 2581 (2019) <https://doi.org/10.3390/s19112581>
16. R.K. Mishra, G.J. Choi, H.J. Choi, J.S. Gwag, ZnS Quantum Dot Based Acetone Sensor for Monitoring Health-Hazardous Gases in Indoor/Outdoor Environment. *Micromachines* **12**, 598 (2021). <https://doi.org/10.3390/mi12060598>
17. L. Zhang, R. Dong, Z. Zhu, S. Wang, Au nanoparticles decorated ZnS hollow spheres for highly improved gas sensor performances. *Sensors and Actuators B* **245**, 112–121 (2017). <http://doi.org/10.1016/j.snb.2017.01.179>
18. L. Chang, X. He, L. Chen, Y. Zhang, Mercaptophenylboronic acid-capped Mn-doped ZnS quantum dots for highly selective and sensitive fluorescence detection of glycoproteins. *Sens Actuators B Chem* **243**, 72–77 (2017). <https://doi.org/10.1016/j.snb.2016.11.121>
19. Z. Bujňáková, E. Dutková, M. Kello, *et al.* Mechanochemistry of Chitosan-Coated Zinc Sulfide (ZnS) Nanocrystals for Bio-imaging Applications. *Nanoscale Res Lett* **12**, 328 (2017). <https://doi.org/10.1186/s11671-017-2103-z>
20. P.A. Ajibade, A.E. Oluwalana, B.M. Sikakane, M. Singh, Structural, photocatalytic and anticancer studies of hexadecylamine capped ZnS nanoparticles. *Chem Phys Lett* **755**, 137813 (2020). <https://doi.org/10.1016/j.cplett.2020.137813>
21. D. Gao, L. Wang, X. Su, *et al.* The role of applied magnetic field in Co-doped ZnS thin films fabricated by pulsed laser deposition. *Opt Mater* **114**, 110877 (2021).

<https://doi.org/10.1016/j.optmat.2021.110877>

22. Y. Piña-Pérez, O. Aguilar-Martínez, P. Acevedo-Peña, et al, Novel ZnS-ZnO composite synthesized by the solvothermal method through the partial sulfidation of ZnO for H₂ production without sacrificial agent. *Appl Catal B Environ* **230**, 125–134 (2018).

<https://doi.org/10.1016/j.apcatb.2018.02.047>

23. Ş. Uzun Çam, T. Serin, A.N. Yazıcı, Effect of Sn doping concentration on structural, optical and electrical properties of ZnS/p-Si (111) diodes fabricated by sol-gel dip-coating method. *Mater Sci Semicond Process* **127**, 105693 (2021). <https://doi.org/10.1016/j.mssp.2021.105693>

24. M. Xin, L.M. Liao, F. Han, Optical properties of ZnS: Ce nanocrystals prepared by hydrothermal method. *J Lumin* **238**, 118074 (2021). <https://doi.org/10.1016/j.jlumin.2021.118074>

25. J.S. Bradley, B. Tesche, W. Busser, et al, Surface Spectroscopic Study of the Stabilization Mechanism for Shape-Selectively Synthesized Nanostructured Transition Metal Colloids. *J Am Chem Soc* **122**, 4631–4636 (2000). <https://doi.org/10.1021/ja992409y>

26. G. Hosseinzadeh, A. Maghari, S.M.F. Farniya, et al, Interaction of insulin with colloidal ZnS quantum dots functionalized by various surface capping agents. *Mater Sci Eng C Mater Biol Appl* **77**, 836–845 (2017). <https://doi.org/10.1016/j.msec.2017.04.018>

27. N. Mohamed, M. Amir, Z. Zaaboub, et al, Effect of temperature and etching under light irradiation on the band edge emission of β -mercaptoethanol-capped CdS colloidal nanocrystals. *J Mater Sci Mater Electron* **31**, 2416–2427 (2020). <https://doi.org/10.1007/s10854-019-02777-w>

28. N. Brahim, M. Poggi, J.C. Lambry, et al, Density of Grafted Chains in Thioglycerol-Capped CdS Quantum Dots Determines Their Interaction with Aluminum(III) in Water. *Inorg Chem* **57**, 4979–4988 (2018). <https://doi.org/10.1021/acs.inorgchem.7b03254>

29. N. Brahim, N. Mohamed, M. Poggi, et al, Interaction of L-cysteine functionalized CdSe quantum dots with metallic cations and selective binding of cobalt in water probed by fluorescence. *Sens Actuators B Chem* **243**, 489–499 (2016). <https://doi.org/10.1016/j.snb.2016.12.003>

30. Y. Yu, L. Xu, J. Chen, H. Gao, S. Wang, J. Fang, S. Xu, Hydrothermal synthesis of GSH–TGA co-capped CdTe quantum dots and their application in labeling colorectal cancer cells, *Colloids Surf. B Biointerfaces*. **95** (2012) 247–253. <https://doi.org/10.1016/j.colsurfb.2012.03.011>.

31. S. Ouni, N. Mohamed, M. Bouzidi, et al, High impact of thiol capped ZnS nanocrystals on the degradation of single and binary aqueous solutions of industrial azo dyes under sunlight. *J Environ Chem Eng* **9**, 105915 (2021). <https://doi.org/10.1016/j.jece.2021.105915>

32. M. Adoni, M. Yadam, S. Gaddam, et al, Antimicrobial, Antioxidant, and Dye Degradation Properties of Biosynthesized Silver Nanoparticles From *Artemisia Annua* L. *Lett Appl NanoBioScience* **10**, 1981–1992, (2021). <https://doi.org/10.33263/LIANBS101.19811992>

33. S. Kannan, N.P. Subiramaniam, M. Sathishkumar, A novel green synthesis approach for improved photocatalytic activity and antibacterial properties of zinc sulfide nanoparticles using plant extract of *Acalypha indica* and *Tridax procumbens*. *J Mater Sci Mater Electron* **31**, 9846–9859 (2020). <https://doi.org/10.1007/s10854-020-03529-x>

34. M. Biruntha, J. Archana, K. Kavitha, et al, Green Synthesis of Zinc Sulfide Nanoparticles Using *Abrus precatorius* and Its Effect on Coelomic Fluid Protein Profile and Enzymatic Activity of the Earthworm, *Eudrilus eugeniae*. *BioNanoScience* **10**, 149–156 (2020). <https://doi.org/10.1007/s12668-019-00694-0>

35. H.R. Rajabi, F. Sajadiasl, H. Karimi, Z.M. Alvand, Green synthesis of zinc sulfide nanophotocatalysts using aqueous extract of *Ficus Johannis* plant for efficient photodegradation of some pollutants. *J Mater Res Technol* **9**, 15638–15647 (2020). <https://doi.org/10.1016/j.jmrt.2020.11.017>

36. S.C. Tudu, J. Kusz, M. Zubko, A. Bhattacharjee, Structural, morphological and optical characterization of green synthesized ZnS nanoparticles using *Azadirachta Indica* (Neem) leaf extract, *Int J Nano Dimens* **11**, 99–111 (2020)

37. R. Belhattab, L. Amor, J.G. Barroso, et al, Essential oil from *Artemisia herba-alba* Asso grown wild in Algeria: Variability assessment and comparison with an updated literature survey. *Arab J*

- Chem **7**, 243–251 (2014). <https://doi.org/10.1016/j.arabjc.2012.04.042>
38. M. Mojarrab, A. Delazar, S. Esnaashari, F.H. Afshar, Chemical composition and general toxicity of essential oils extracted from the aerial parts of *Artemisia armeniaca* Lam. and *A. incana* (L.) Druce growing in Iran. *Res Pharm Sci* **8**:65–69 (2013)
39. A. Asdadi, A. Hamdouch, S. Gharby, and L. M. I. Hassani, *Journal of Analytical Sciences and Applied Biotechnology* **2**, 2 (2020). <https://doi.org/10.48402/IMIST.PRSM/jasab-v2i2.21589>
40. K.S. Bora, A. Sharma, The Genus *Artemisia*: A Comprehensive Review. *Pharm Biol* **49**, 101–109 (2011). <https://doi.org/10.3109/13880209.2010.497815>
41. Y. Aniya, M. Shimabukuro, M. Shimoji, et al, Antioxidant and Hepatoprotective Actions of the Medicinal Herb *Artemisia campestris* from the Okinawa Islands. *Biol Pharm Bull* **23**, 309–312 (2000). <https://doi.org/10.1248/bpb.23.309>
42. M.J. Abad, L.M. Bedoya, L. Apaza, P. Bermejo, The *Artemisia* L. Genus: A Review of Bioactive Essential Oils. *Molecules* **17**, 2542–2566 (2012). <https://doi.org/10.3390/molecules17032542>
43. T. El-lamey, A. Kamel, and E. Elsharkawy, Volatile oils content of some species of *Artemisia* growing under different environmental conditions and its effect on germination of seeds of some plants, *IOSR Journal of Agriculture and Veterinary Science* **11**, 83 (2018). <https://doi.org/10.9790/2380-1112028393>
44. P. Parameswari, R. Devika, and P. Vijayaraghavan, *In vitro* anti-inflammatory and antimicrobial potential of leaf extract from *Artemisia nilagirica* (Clarke) Pamp, *Saudi Journal of Biological Sciences* **26**, 460 (2019). <https://doi.org/10.1016/j.sjbs.2018.09.005>
45. H. Dai, N. Feng, J. Li, et al, Chemiresistive humidity sensor based on chitosan/zinc oxide/single-walled carbon nanotube composite film. *Sens Actuators B Chem* **283**, 786–792 (2019). <https://doi.org/10.1016/j.snb.2018.12.056>
46. I. Aranaz, A.R. Alcántara, M.C. Civera, et al, Chitosan: An Overview of Its Properties and Applications. *Polymers* **13**, 3256 (2021). <https://doi.org/10.3390/polym13193256>
47. F. Zouaoui, S. Bourouina-Bacha, M. Bourouina, et al, Electrochemical sensors based on molecularly imprinted chitosan: A review. *TrAC Trends Anal Chem* **130**, 115982 (2020). <https://doi.org/10.1016/j.trac.2020.115982>
48. Y. Jiang, J. Wu, Recent development in chitosan nanocomposites for surface-based biosensor applications. *Electrophoresis* **40**, 2084–2097 (2019). <https://doi.org/10.1002/elps.201900066>
49. F.I.M. Ali, S.T. Mahmoud, F. Awwad, et al, Low power consumption and fast response H₂S gas sensor based on a chitosan-CuO hybrid nanocomposite thin film. *Carbohydr Polym* **236**, 116064 (2020). <https://doi.org/10.1016/j.carbpol.2020.116064>
50. N.L. Lukman Hekiem, A.A. Md Ralib, M.A. Mohd Hatta, et al, Effect of chitosan dissolved in different acetic acid concentration towards VOC sensing performance of quartz crystal microbalance overlay with chitosan. *Mater Lett* **291**, 129524 (2021). <https://doi.org/10.1016/j.matlet.2021.129524>
51. A. Madaci, G. Raffin, M. Hangouet, et al, A microconductometric ethanol sensor prepared through encapsulation of alcohol dehydrogenase in chitosan: application to the determination of alcoholic content in headspace above beverages. *J Mater Sci Mater Electron* **32**, 17752–17763 (2021). <https://doi.org/10.1007/s10854-021-06311-9>
52. D. Amaranatha Reddy, C. Liu, R.P. Vijayalakshmi, B.K. Reddy, Effect of Al doping on the structural, optical and photoluminescence properties of ZnS nanoparticles. *J Alloys Compd* **582**, 257–264 (2014). <https://doi.org/10.1016/j.jallcom.2013.08.051>
53. H. Asoufi, T. Al-Antary, A. Awwad, Biosynthesis and characterization of iron sulfide (FeS) nanoparticles and evaluation their aphicidal activity on the green peach aphid *myzus persicae* (Homoptera: aphididae). *Fresenius Environ Bull* **27**:7767–7775 (2018)
54. Q.F. Nafa, S.M. Hussin, W.F. Hamadi, Characterization of some active organic compound from Cold and Hot aqueous solvent and Study their Antibiotic of *Artemisia herba-alba* Asso plant oil. *Egypt J Chem* **64**, 6691–6709 (2021). <https://doi.org/10.21608/ejchem.2021.72074.3587>
55. U.S. Senapati, D. Sarkar, Structural, spectral and electrical properties of green synthesized ZnS

- nanoparticles using *Elaeocarpus floribundus* leaf extract. *J Mater Sci Mater Electron* **26**, 5783–5791 (2015). <https://doi.org/10.1007/s10854-015-3137-6>
56. Y. Yu, L. Xu, J. Chen, et al, Hydrothermal synthesis of GSH–TGA co-capped CdTe quantum dots and their application in labeling colorectal cancer cells. *Colloids Surf B Biointerfaces* **95**, 247–253 (2012). <https://doi.org/10.1016/j.colsurfb.2012.03.011>
57. M. Jothibas, C. Manoharan, S. Johnson Jeyakumar, et al, Synthesis and enhanced photocatalytic property of Ni doped ZnS nanoparticles. *Sol Energy* **159**, 434–443 (2018). <https://doi.org/10.1016/j.solener.2017.10.055>
58. B. Poornaprakash, U. Chalapathi, Y. Suh, et al, Terbium-doped ZnS quantum dots: Structural, morphological, optical, photoluminescence, and photocatalytic properties. *Ceram Int* **44**, 11724–11729 (2018). <https://doi.org/10.1016/j.ceramint.2018.03.250>
59. S. Ouni, N.B.H. Mohamed, N. Chaaben, et al, Fast and effective catalytic degradation of an organic dye by eco-friendly capped ZnS and Mn-doped ZnS nanocrystals. *Environ Sci Pollut Res* **29**, 33474–33494 (2022). <https://doi.org/10.1007/s11356-021-17860-1>
60. V. Mote, Y. Purushotham, B. Dole, Williamson–Hall analysis in estimation of lattice strain in nanometer-sized ZnO particles. *J Theor Appl Phys* **6**, 6 (2012). <https://doi.org/10.1186/2251-7235-6-6>
61. H. Matsumoto, T. Sakata, H. Mori, H. Yoneyama, Preparation of Monodisperse CdS Nanocrystals by Size Selective Photocorrosion. *J Phys Chem* **100**:13781–13785 (1996). <https://doi.org/10.1021/jp960834x>
62. A. Iqbal, U. Saidu, F. Adam, S. Sreekantan, N. Jasni, and M. N. Ahmad, The Effects of Zinc Oxide (ZnO) Quantum Dots (QDs) Embedment on the Physicochemical Properties and Photocatalytic Activity of Titanium Dioxide (TiO₂) Nanoparticles, *JPS* **32**, 71 (2021). <https://doi.org/10.21315/jps2021.32.2.6>
63. N. Ben Brahim, M. Poggi, N.B. Haj Mohamed, et al, Synthesis, characterization and spectral temperature-dependence of thioglycerol–CdSe nanocrystals. *J Lumin* **177**, 402–408 (2016). <https://doi.org/10.1016/j.jlumin.2016.05.026>
64. J.R. Snider, G.A. Dawson, Tropospheric light alcohols, carbonyls, and acetonitrile: Concentrations in the southwestern United States and Henry’s Law data. *J Geophys Res Atmospheres* **90**, 3797–3805 (1985). <https://doi.org/10.1029/JD090iD02p03797>
65. R. Sander, Compilation of Henry’s Law Constants for Inorganic and Organic Species of Potential Importance in Environmental Chemistry, version 3, 8 Apr 1999 <http://www.mpch-mainz.mpg.de/~sander/res/henry.html> Errata (collected from the above web site 4 June 2003) Wel. H - PHA KH H - PHA Thanks J C Wheel
66. N. Lavanya, S.G. Leonardi, S. Marini, et al, MgNi₂O₃ nanoparticles as novel and versatile sensing material for non-enzymatic electrochemical sensing of glucose and conductometric determination of acetone. *J Alloys Compd* **817**, 152787 (2020). <https://doi.org/10.1016/j.jallcom.2019.152787>
67. R. Krishna, J.M. Van Baten, Water/Alcohol Mixture Adsorption in Hydrophobic Materials: Enhanced Water Ingress Caused by Hydrogen Bonding. *ACS Omega* **5**, 28393–28402 (2020). <https://doi.org/10.1021/acsomega.0c04491>
68. C.F. Fong, C.L. Dai, C.C. Wu, Fabrication and Characterization of a Micro Methanol Sensor Using the CMOS-MEMS Technique. *Sensors* **15**, 27047–27059 (2015). <https://doi.org/10.3390/s151027047>
69. Q. Liu, J.R. Kirchhoff, Amperometric detection of methanol with a methanol dehydrogenase modified electrode sensor. *J Electroanal Chem* **601**, 125–131 (2007). <https://doi.org/10.1016/j.jelechem.2006.10.039>
70. J. Van den Broek, S. Abegg, S.E. Pratsinis, A.T. Güntner, Highly selective detection of methanol over ethanol by a handheld gas sensor. *Nat Commun* **10**, 4220 (2019). <https://doi.org/10.1038/s41467-019-12223-4>
71. K. Phasukom, W. Prissanaroon-Ouajai, A. Sirivat, A highly responsive methanol sensor based on graphene oxide/polyindole composites. *RSC Adv* **10**, 15206–15220 (2020).

<https://doi.org/10.1039/D0RA00158A>

72. Y. Li, D. Deng, X. Xing, et al, A high performance methanol gas sensor based on palladium-platinum-In₂O₃ composited nanocrystalline SnO₂. *Sens Actuators B Chem* **237**, 133–141 (2016).

<https://doi.org/10.1016/j.snb.2016.06.088>

73. B. Mandal, Aaryashree, R. Singh, S. Mukherjee, Highly Selective and Sensitive Methanol Sensor Using Rose-Like ZnO Microcube and MoO₃ Micrograss-Based Composite. *IEEE Sens J* **18**, 2659–2666 (2018). <https://doi.org/10.1109/JSEN.2018.2803682>

74. D. Acharyya, S. Acharyya, K. Huang, et al, Highly Sensitive ppb Level Methanol Sensor by Tuning C:O Ratio of rGO-TiO₂ Nanotube Hybrid Structure. *IEEE Trans Nanotechnol* **16**, 1122–1128 (2017).

<https://doi.org/10.1109/TNANO.2017.2764124>

75. K. Phasukom, W. Prissanaroon-Ouajai, A. Sirivat, Electrical conductivity response of methanol sensor based on conductive polyindole. *Sens Actuators B Chem* **262**, 1013–1023 (2018).

<https://doi.org/10.1016/j.snb.2018.02.088>

76. I. Musa, G. Raffin, M. Hangouet, et al, Electrospun PVC-nickel phthalocyanine composite nanofiber based conductometric methanol microsensor. *Microchem J* **182**, 107899 (2022b).

<https://doi.org/10.1016/j.microc.2022.107899>

77. I. Musa, G. Raffin, M. Hangouet, et al, Development of a Chitosan/Nickel Phthalocyanine Composite Based Conductometric Micro-sensor for Methanol Detection. *Electroanalysis* **34**, 1338–1347 (2022a). <https://doi.org/10.1002/elan.202100707>

78. A.A. Athawale, S.V. Bhagwat, P.P. Katre, Nanocomposite of Pd–polyaniline as a selective methanol sensor. *Sens Actuators B Chem* **114**, 263–267 (2006).

<https://doi.org/10.1016/j.snb.2005.05.009>

Supplementary Information

A novel conductometric micro-sensor for methanol detection based on chitosan/Zinc sulfur-nanoparticles composite obtained by green synthesis

S. Ouni ^{a,b*}, Naim Bel Haj Mohamed ^{c*}, M. Haouari ^b, Abdelhamid Elaissari ^a, Abdelhamid Errachid ^a, and Nicole Jaffrezic-Renault ^{a*}

^a Institute of Analytical Sciences, University of Lyon, 69100 Villeurbanne, France

^b Laboratory of Advanced Materials and Interfaces (LIMA), University of Monastir, Faculty of Sciences of Monastir, Monastir-Tunisia

^c Research Unit on Hetero-Epitaxies and Applications, Faculty of Sciences of Monastir, University of Monastir, Avenue of the Environment, 5019 Monastir, Tunisia

*Corresponding authors E-mail: nicole.jaffrezic@univ-lyon1.fr

Experimental section

1. Chemicals and Reagents

Analytical grade chemicals were used from commercial sources without any further purification. Zinc (II) acetate dihydrate ($\text{Zn} [\text{CH}_3\text{COO}]_2 \cdot 2\text{H}_2\text{O} \geq 98\%$), sodium sulfide ($\text{Na}_2\text{S} \geq 98\%$), sodium hydroxide (NaOH , 99%), Chitosan lower molecular weight (deacetylated chitin, degree of acetylation 85-95% Mw=230 kDa) and glacial acetic acid (99.9%) were purchased from Sigma-Aldrich. Ultra-pure water (UPW) from Millipore System was employed in all aqueous solutions (resistivity >18 MOhm.com).

2. Artemisia Herba Alba extraction

Artemisia Herba Alba (AHA) leaves were collected in Tunisia. The selected parts of AHA plants were washed with deionized water, dried in the shade at room temperature, and ground into powder. 11.5 g of powder was added to 200 mL of distilled water. The mixtures were boiled at 100 °C for 2h and filtrated at room temperature. The filtrated aqueous solution is the extract of A. herba-alba, which is used for ZnS nanoparticle fabrication in the present study.

Fig. S1 shows a picture of A. herba-alba leaves and their extract.



Fig.S1: Artemisia Herba Alba plant and its extract.

3. Synthesis of AHA-capped ZnS NPs

The detailed preparation method of ZnS nanoparticles was reported elsewhere using the colloidal wet chemical route [1,2]. *Artemisia Herba Alba* (AHA) was used as a stabilizer for preparing the green ZnS NPs. The typical synthesis process of AHA capped ZnS NPs is the following one: 20ml of *Artemisia Herba Alba* aqueous extract were mixed with 3mM of Zn[OOCCH₃]₂·2H₂O solution. The mixture was agitated and degassed in the presence of N₂ for 30 min. In a second step, 1.2 mM of Na₂S solution was added to the solution containing Zn-AHA complexes at room temperature under stirring. Then, the mixture was heated under N₂ reflux at 100 °C for 3 h to obtain the final AHA-capped ZnS NPs.

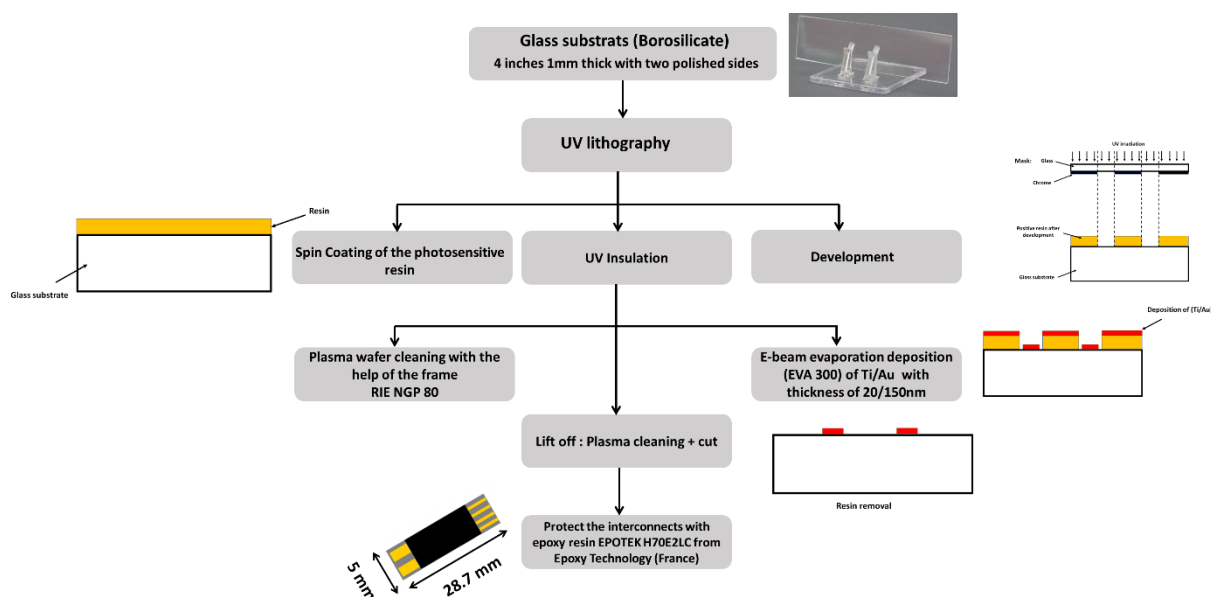
In general, a temperature of 100°C is commonly used in hydrothermal synthesis because it is a relatively mild temperature that can be achieved using simple laboratory equipment, while still being high enough to promote the desired chemical reactions. Additionally, 100°C is close to the boiling point of water, which means that the solution can be maintained in a liquid state, avoiding issues with evaporation and loss of solvents. Furthermore, at 100°C, the reaction rate is fast enough to produce nanoparticles within a reasonable time frame, but not so fast that it becomes difficult to control the size, shape, and composition of the particles. This makes it an ideal temperature for the synthesis of a wide range of nanoparticle types, including metal oxides, sulfides, and hydroxides. Overall, 100°C is a commonly used temperature in hydrothermal synthesis due to its ease of use, controllability, and suitability for a wide range of nanoparticle synthesis applications. The 3 h of synthesis is chosen after preliminary study to fix to optimum conditions like time, molar ratio and pH. It was confirmed that maximum of photoluminescence intensity was obtained with 3 h of synthesis with is very important in applications of our nanoparticles like the photocatalysis activity [3].

The dried precipitate was allowed to cool down naturally at room temperature in order to stop the growth of NPs. A nanocolloidal suspension was formed and centrifuged at 2500 rpm for 20 min; After removing the supernatant and replacing it with ethanol, the suspension was cen-

trifuged, and after removing the supernatant, the obtained nanoparticles were stored at room temperature.

4. Fabrication process and packaging of micro-conductometric chips

The interdigitated microelectrode chip was fabricated using UV lithography and thin film e-beam evaporation deposition. The fabrication procedures were carried out at the Institute of Nanotechnology of Lyon (INL), Lyon, France. **The size of the interdigitated chip was 5x 28.7 mm. Finger width was 20 μm , the finger distance was also 20 μm .** The flowchart for the pro-



cess of fabrication of the microconductometric chip is presented in **Fig. S2**.

Fig.S2: Flow-chart for the process of fabrication of microconductometric chips

5. Electrodeposition of chitosan/ZnS-AHA films on the interdigitated electrodes

The fabricated microelectrode chips were cleaned through sonicating in ethanol for 15 min, in acetone for 15 min, rinsed in water, dried under a nitrogen flow, and then exposed to UV-Ozone Pro Cleaner (BioForce) for 30 min before electrodeposition of chitosan/ZnS-AHA on the electrode surfaces. The chemical composition of the ZnS-AHA NPs suspension was: 1%

(v/v) of acetic acid, 1% (w/w) of chitosan; (lower molecular weight). The pH was adjusted at 7 by carefully adding drops of 0.1M NaOH into the chitosan suspension while agitating using a magnetic. The electrodeposition process for the fabrication of the conductimetric sensor is presented in **Fig. S3**.

For the chronoamperometric deposition technique, a three-electrode format was used: the working sensor as a working electrode, an Ag/AgCl as reference electrode, and a platinum wire as counter electrode. The next step was carried out by putting the three electrodes in a 5 mL beaker of Chitosan + ZnS NPs solution (working electrode). The chronoamperometric deposition was conducted at an applied potential of -1.4 V for 4 min by using an EC LAB potentiostat [3]. The cathodic current at the electrode, measured as a function of time, fluctuated according to the diffusion of H^+ from the bulk solution towards the sensor surface. The current (mA) continued to decrease until it became stable within 4 min, which assumes the (chitosan/chitosan + NPs) film is well deposited on the gold surface to form a film. **A current of 50 μA is observed through the proton reduction, and then a decrease in this current is observed, due to the deposition of the chitosan (chitosan/ZnS-NPs) film on the interdigitated electrodes (IDEs). A stable value of 3 μA is observed after the first minute (Fig. S4).** The same procedure is used for the reference sensor, a chitosan film is deposited without ZnS-NPs. After electrodeposition, the chips were carefully rinsed in ultrapure water (UPW), kept dry in air for 45 min, and then stored in the fridge at 4 °C before use. The fabricated sensor from chitosan/ZnS-AHA is ready for gas detection using conductometric measurements in the differential mode.

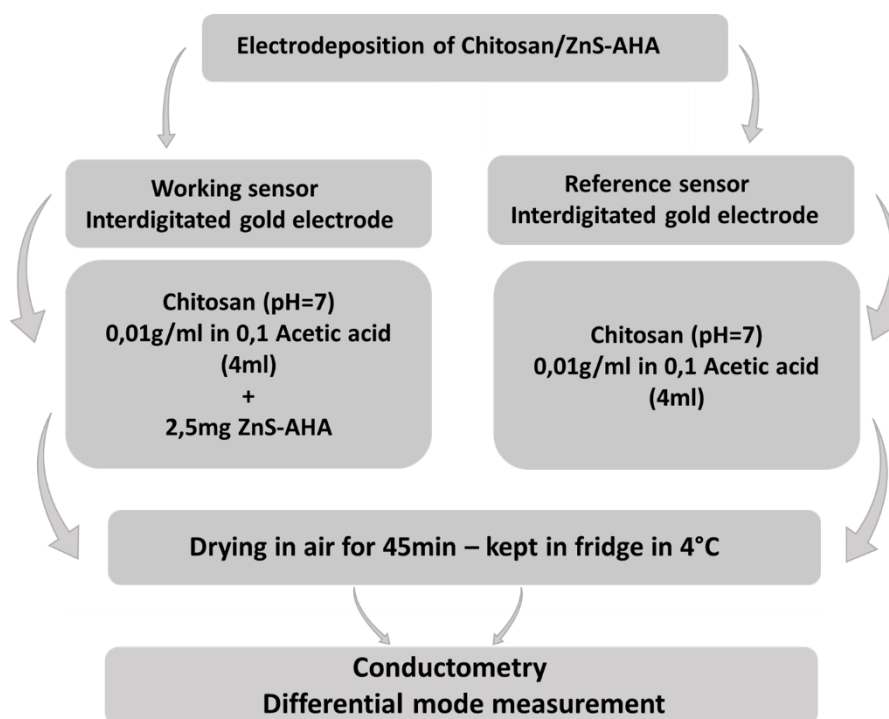


Fig. S3: Flow-chart for the process of fabrication of microconductometric chips

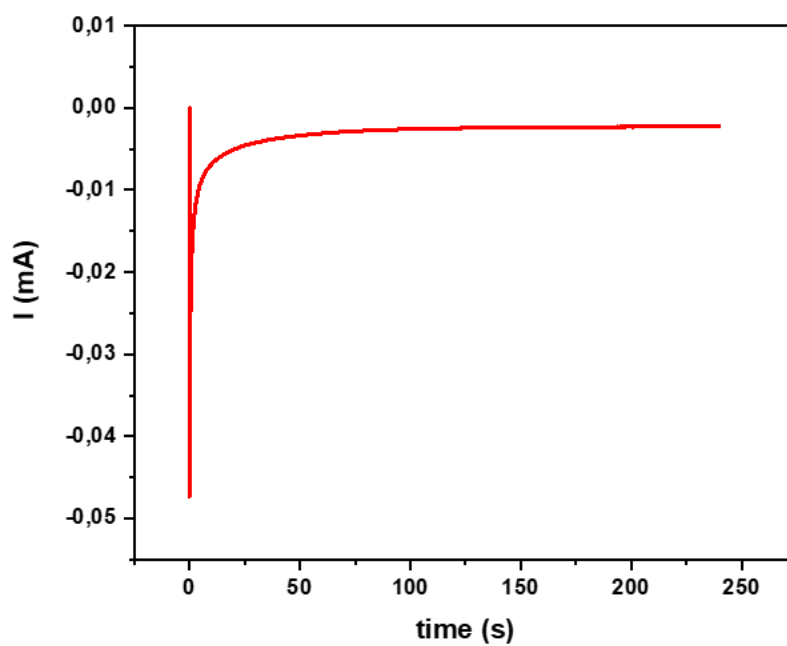


Fig. S4: Chronoamperometric measurement monitoring of electrodeposition of chitosan

6. Characterization techniques

Various techniques were applied to characterize AHA-capped ZnS NPs. XRD measurements were performed using Panalytical X' Pert Pro diffractometer with a $\text{CuK}\alpha$ radiation source ($\lambda=1,542\text{\AA}$).

The Fourier transform infrared (FTIR) spectrum of ZnS-AHA NPs was obtained in the transmission mode at room temperature using a Perkin Elmer version 5.3 spectrophotometer in the spectral range of $400\text{--}4000\text{ cm}^{-1}$ using KBr pellet disks.

HR-TEM images were obtained using a JEM-2100 analytical electron microscope operating at an accelerating voltage of 200 kV and equipped with an Energy Dispersive X-ray (EDX) system for elemental chemical analysis. A drop of nanocrystal solution was poured on carbon-coated copper grids to obtain HR-TEM samples after the excess solvent was evaporated. **The nanocrystal size and size distribution data were obtained based on the HR-TEM images by measuring at least 100 randomly selected nanocrystals using an image processing program (ImageJ, version 1.50).**

SEM images were obtained using a Tescan Vega SBU scanning electron microscope, operating at an accelerating voltage of 20 kV, equipped with a Bruker Esprit Compact EDS detector.

Absorbance spectra were recorded using a SPECORD 210 Plus spectrophotometer with a quartz cuvette in the range of 200-800 nm at room temperature. Photoluminescence (PL) spectroscopy was applied to analyze the defects and emission properties of the ZnS using as exciting source the 325 nm of a helium-cadmium laser source.

7. Conductometric measurements

Conductometric detection was achieved by applying to each pair of interdigitated electrodes (sensors) a small-amplitude sinusoidal voltage (10 mV peak-to-peak at 0 V) at a 10 kHz frequency generated by "VigiZMeter" conductometer which is manufactured by the company "Covarians", and the responses of the gas sensor were recorded as a function of time. These conditions were used to reduce faradaic processes, multi-layer charging, and polarization at the microelectrode surface [4]. The differential output signal was recorded between the working and the reference pairs of interdigitated electrodes. The working sensor was obtained by electro-deposition of a chitosan/ZnS-AHA NPs film and the reference sensor was obtained by the electro-deposition of a chitosan film. **Conductometric measurements were done by introducing the working sensor and the reference sensor in the headspace over the liquid phase in a cylindrical container for one minute and then by withdrawing it (Fig. S5).** The differential measurement of conductance (ΔG) was recorded versus time. The response time (t_{Res}) des-

cribes the time necessary to reach 90% of the total change of conductance and the recovery time (t_{Rec}) characterizes the time necessary to recover 10% of the total change in conductance.

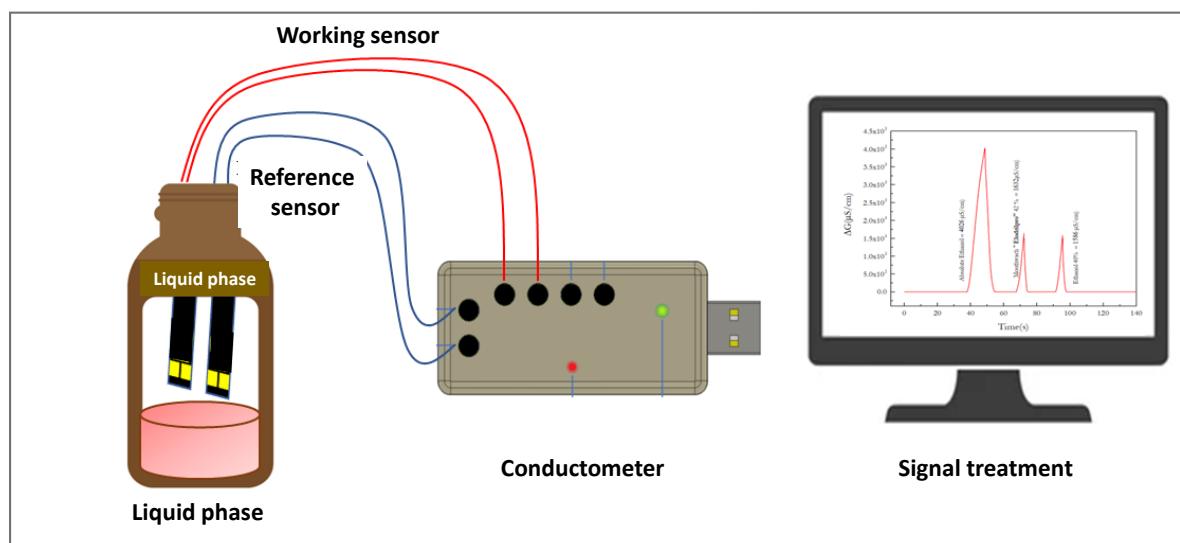


Figure S5. Diagram of the experimental setup

8. Preparation of VOC samples

The gas sensor performance was tested methanol, ethanol and acetone samples which were collected from the headspace above aqueous solutions with known concentrations of (0-100%). The as-mentioned gas phase concentration depends on Henry's law constants of the given analyte in water and was calculated from Henry's law following the equation announced at 25°C by Sander in 1999 [4].

$$k_H^0 = \frac{c_a}{p_g} \quad (4)$$

Where k_H^0 is the Henry's law constant for standard conditions; $[k_H^0] = \text{M/atm}$, c_a is the aqueous concentration of the analyte; $[c_a] = \text{M}$ and p_g is the partial pressure of the analyte in the gas phase; $[p_g] = \text{atm}$.

For the gas analytes listed above at (25°C) i.e, methanol, ethanol, and acetone; the Henry's law constants value of $2.2 \times 10^2 \text{ M/atm}$, $1.9 \times 10^2 \text{ M/atm}$, and $0.24 \times 10^2 \text{ M/atm}$ were considered respectively [5]. In **Table S1**, the calculated equilibrium gas-phase concentrations of methanol, ethanol and acetone above the aqueous phase are listed.

Table S1: Equilibrium gaseous phase concentrations above aqueous methanol, ethanol, and acetone solution at 25 °C per Henry’s law constants reported by Sander et al [5].

S/N	% Volumetric concentration	Concentration of methanol in the gaseous phase (% v/v)	Concentration of ethanol in the gaseous phase (%v/v)	Concentration of acetone in the gaseous phase (% v/v)
1	0%	0	0	0
2	20%	2.25	1.79	11.26
3	40%	4.5	3.58	22.52
4	60%	6.75	5.37	33.78
5	80%	9	7.16	45.04
6	100%	11.25	8.95	56.03

6. Selectivity of the methanol detection

To confirm the sensor selectivity, in addition of the methanol/water solutions we have tested the Measurement of methanol when ethanol and acetone are presented. From **Fig. S5**, it is observed that the methanol signal is increased by a factor of 10% in the presence of ethanol (2%) and by a factor of 4 % in the presence of acetone (2%).

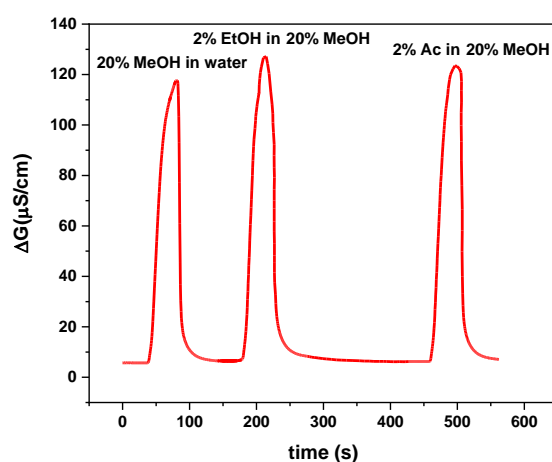


Fig. S5: Effect of the presence of 1/5 of ethanol and of acetone compared to methanol on the sensor signal

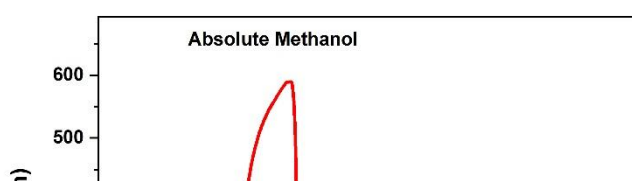


Fig. S6: Detection of gas-phase concentrations for different methanol/water solutions and commercial ice washer product, with the chitosan/ZnS-NPs sensor

References

1. S. Ouni, N. Mohamed, M. Bouzidi, et al, High impact of thiol capped ZnS nanocrystals on the degradation of single and binary aqueous solutions of industrial azo dyes under sunlight. *J Environ Chem Eng* **9**, 105915 (2021). <https://doi.org/10.1016/j.jece.2021.105915>
2. S. Ouni, N.B.H. Mohamed, N. Chaaben, et al, Fast and effective catalytic degradation of an organic dye by eco-friendly capped ZnS and Mn-doped ZnS nanocrystals. *Environ Sci Pollut Res* **29**, 33474–33494 (2022). <https://doi.org/10.1007/s11356-021-17860-1>
3. S. Ouni, N.B.H. Mohamed, M. Haouari, A. Elaissari, Abdelhamid Errachid, N. Jaffrezic- Renault, A Novel Green Synthesis of Zinc Sulfide Nano- Adsorbents Using Artemisia Herba Alba Plant Extract for Adsorption and Photocatalysis of Methylene Blue Dye. *Chemistry Africa*. <https://doi.org/10.1007/s42250-023-00667-7>
4. A. Madaci, G. Raffin, M. Hangouet, et al, A microconductometric ethanol sensor prepared through encapsulation of alcohol dehydrogenase in chitosan: application to the determination of alcoholic content in headspace above beverages. *J Mater Sci Mater Electron* **32**, 17752–17763 (2021). <https://doi.org/10.1007/s10854-021-06311-9>
5. R. Sander, Compilation of Henry's Law Constants for Inorganic and Organic Species of Potential Importance in Environmental Chemistry, version 3, 8 Apr 1999 <http://www.mpch-mainz.mpg.de/~sander/res/henry.html> Errata (collected from the above web site 4 June 2003) Wel. H - PHA KH H - PHA Thanks J C Wheel
6. J.R. Snider, G.A. Dawson, Tropospheric light alcohols, carbonyls, and acetonitrile: Concentrations in the southwestern United States and Henry's Law data. *J Geophys Res Atmospheres* **90**, 3797–3805 (1985). <https://doi.org/10.1029/JD090iD02p03797>